TB, DC, PMB/231011, 21/12/2006

INSTITUTE OF PHYSICS PUBLISHING PHYSICS IN MEDICINE AND BIOLOGY

Phys. Med. Biol. **52** (2007) 1–21 UNCORRECTED PROOF

Lenses and effective spatial resolution in macroscopic optical mapping

Harold Bien[1], **Puja Parikh**[1] **and Emilia Entcheva**[1,2]

[1] Department of Biomedical Engineering, Stony Brook University, Stony Brook, NY 11794-8181, USA
[2] Department of Biophysics and Physiology, Stony Brook University, Stony Brook, NY 11794-8181, USA

E-mail: emilia.entcheva@sunysb.edu

Received 18 August 2006, in final form 2 December 2006
Published DD MMM 2006
Online at stacks.iop.org/PMB/52/1

Abstract

Optical mapping of excitation dynamically tracks electrical waves travelling through cardiac or brain tissue by the use of fluorescent dyes. There are several characteristics that set optical mapping apart from other imaging modalities: dynamically changing signals requiring short exposure times, dim fluorescence demanding sensitive sensors and wide fields of view (low magnification) resulting in poor optical performance. These conditions necessitate the use of optics with good light gathering ability, i.e. lenses having high numerical aperture. Previous optical mapping studies often used sensor resolution to estimate the minimum spatial feature resolvable, assuming perfect optics and infinite contrast. We examine here the influence of finite contrast and real optics on the *effective* spatial resolution in optical mapping under broad-field illumination for both lateral (in-plane) resolution and axial (depth) resolution of collected fluorescence signals.

(Some figures in this article are in colour only in the electronic version)

1. Introduction

Optical mapping of excitable tissue using fluorescent dyes has made it possible to directly test scientific predictions regarding cardiac arrhythmias (Efimov *et al* 2004) and neural activity for visual processing (Polimeni *et al* 2005). Capitalizing on the key benefit of optical mapping, namely measurements at high spatial resolution, requires systems with suitably high pixel counts over a wide field of view (low magnification). Such conditions set apart optical mapping from other more traditional imaging modalities due to the unique combination of low light fluorescence signals, rapidly changing images and optics used in sub-optimal conditions (Entcheva and Bien 2006). Unlike photography or cinematography

where inadequate resolution is readily discerned, no indications are available when optical mapping fails to accurately represent the underlying specimen. Understanding the spatial limit of optical mapping is critical in the proper interpretation of data—overestimation gives the false impression of homogeneity when there really is none; underestimation may cause one to aggressively filter out fine spatial features. Recent reports of low spatial frequency in optical mapping of heart tissue (Mironov *et al* 2006) and controversy surrounding the true spatial limits in neural optical mapping (Polimeni *et al* 2005) naturally lead to the question: what is the 'true' spatial resolution of an optical mapping system?

The ability to resolve fine spatial detail is often represented as the diffraction limit for microscopy or the effective pixel size (physical size of each sensor pixel scaled by optical magnification) for macroscopic imaging. However, these measures reflect only the upper bound of spatial resolution as they assume ideal conditions of infinite contrast and perfect optics. For the more realistic case of finite contrast, actual spatial resolution can also be limited by inability to distinguish the difference in intensity between the object and its background, i.e. poor contrast (Smith 1990). As physical pixel sizes shrink in modern detectors (Entcheva and Bien 2006), the weakly contrasting images of optical mapping due to dim fluorescence aggravated by short exposure times might limit spatial resolving ability rather than pixel size.

Contrast-limited imaging has several important implications for spatial resolution. First, optical components such as lenses can degrade contrast and thus impact resolution. Second, the minimum detectable contrast depends upon the sensor's ability to represent varying intensities as unique digital greyscale levels—a factor not often considered in determination of spatial resolution. Third, the actual resolving ability of an imaging system is a function of the contrast of the object being imaged—for optical mapping, this means constantly changing resolution. In the extreme case where the intensity differences over the entire field of view (FOV) are degraded below the intensity resolution (dynamic range) of the sensor by the imaging optics, resolving ability becomes nil and resolution indeterminate.

When imaging relatively thick specimens, e.g. whole heart or three-dimensional tissue slabs, consideration must also be given to how three-dimensional objects' fluorescence projects onto planar imaging sensors. Experimental studies and simulations (Baxter *et al* 2001, Ding *et al* 2001, Ramshesh and Knisley 2003, Bray and Wikswo 2003, Bernus *et al* 2005, Bishop *et al* 2006) on the depth of fluorescence collected by a planar imaging system have focused primarily on photon scattering and absorption properties of the tissue assuming ideal sensors with full-scale dynamic range responses (infinite contrast). Unlike planar resolution, axial (depth) resolution is almost always limited by contrast unless special care is taken to block out-of-focus light, e.g. confocal imaging. Thus, optics along with light–tissue interactions is expected to substantially affect axial resolution.

We report here a relatively simple method for empirically estimating the effective spatial resolution of a contrast-limited optical mapping system with broad-field illumination. We show how even high performance ('fast') lenses can degrade contrast and hence resolution, and explore the benefits of tandem-lens constructs. Using simple geometric models and empirical tests, we also examine the effect of various optical mapping parameters on axial resolution.

2. Background and model details

2.1. Spatial resolution and contrast

Spatial *resolution* in imaging is defined as the system's ability to reproduce object detail. The highest resolvable spatial frequency in the imaging plane will depend on the pixel size

of the detector and the Nyquist criterion (requiring at least two times higher sampling than the signal), while the spatial resolution in the object plane will be inversely scaled by the magnification used. However, resolution as a single number implies infinite contrast; changes in image *contrast* can affect image resolution. Contrast transfer function (CTF) and modulation transfer function (MTF) have been adopted for quantifying the quality of an imaging system or system component (e.g. lens or sensor) in terms of contrast loss over a range of spatial frequencies (Smith 1990). CTF and MTF differ in the target used to form an image—the response to a black/white binary pattern with sharp transitions is described by the former, while the later is quantified by response to spatial frequencies with sinusoidal modulation of intensity. Both of these characteristics can be calculated theoretically as the amplitude of the Fourier transform of a line spread function for known optical component characteristics or can be obtained empirically using special test patterns with varying spatial frequency. MTF and CTF are linked through the harmonics of the spatial frequency (ν) via equation (1) (Coltman 1954). For relatively high spatial frequencies, the relationship can be further simplified to equation (2).

$$\%\mathrm{MTF} = \frac{\pi}{4}\left[\mathrm{CTF}(\nu) + \frac{\mathrm{CTF}(3\nu)}{3} + \frac{\mathrm{CTF}(5\nu)}{5} + \cdots\right] \tag{1}$$

$$\%\mathrm{MTF} = 0.785 * \mathrm{CTF}(\nu). \tag{2}$$

For an idealized, simple (thin) lens, the resolution is limited by diffraction effects and can be quantified through a monochromatic diffraction-limited modulation transfer function (MDMTF). For a monochromatic source, the MDMTF can be computed for a lens with numerical aperture *NA* and wavelength λ (Smith 1990):

$$\begin{aligned} \mathrm{MDMTF}(\nu) &= \frac{2}{\pi}(\phi - \cos\phi \sin\phi) \\ \phi &= \cos^{-1}\left(\frac{\lambda\nu}{2NA}\right). \end{aligned} \tag{3}$$

Empirically obtained MTF and CTF curves can be used to predict the spatial frequency at which the imaging system loses sufficient contrast and reaches the practical limit of spatial resolution. The limiting contrast is a function of the amplitude of the original signal (S_{p-p}) and any noise (σ) present in the system. When the degraded signal amplitude falls below the noise level, the spatial feature can no longer be resolved as distinct from the background noise:

$$\mathrm{MTF}(\nu) \times S_{p-p} \geqslant \sigma. \tag{4}$$

In the limiting case of a noise-free system, the minimum acceptable contrast will be defined by the bit resolution of the imaging sensor such that the effective contrast, $\mathrm{MTF}(\nu) \times S_{p-p}$, must resolve to at least 1 greyscale level (GL). The highest spatial frequency resolvable by a system, $\nu_{\max}$, is found for MTF equal to the inverse of the signal-to-noise ratio (SNR) or of the S_{p-p} in the case of no noise, equation (5), and forms the basis of what we term *effective* spatial resolution $\delta x_{\min} = \frac{1}{\nu_{\max}}$.

$$\mathrm{MTF}(\nu_{\max}) = \begin{cases} \left\lceil \dfrac{\sigma}{S_{p-p}} \right\rceil = \left\lceil \dfrac{1}{\mathrm{SNR}} \right\rceil, & \text{if} \quad \sigma \geqslant 1 \\ \left\lceil \dfrac{1}{S_{p-p}} \right\rceil & \text{otherwise.} \end{cases} \tag{5}$$

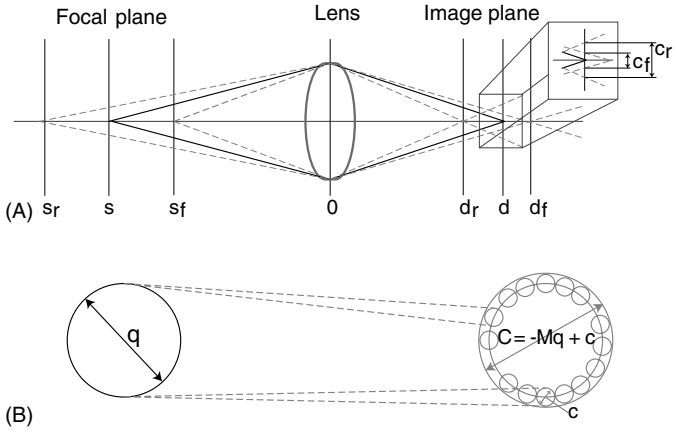

Figure 1. Schematic illustration of the 'circle of confusion' concept. (A) Point sources away from the focal plane project as conical sections, i.e. circles, in the imaging plane. The lens is located at position 0 and the focal plane is at position s in front of the lens with the corresponding image plane at position d behind the lens. Point sources behind the focal plane at s_r would project to a point at d_r and similarly point sources in front of the focal plane (s_f) would project onto d_f. The inset shows the resulting line of length c_f or c_r at the in-focus imaging plane, d. Rotation about the central axis would then yield a filled circle of diameters c_f and c_r. (B) A finite circle of diameter q will appear as a larger circle with diameter $C = -Mq + c$ when positioned away from the focal plane.

2.2. Axial spatial resolution (ASR) versus lateral spatial resolution (LSR)

Optical mapping of three-dimensional tissue is affected by the extent (depth) of tissue from which fluorescence is collected, often termed 'depth of field'. There are various estimates of 'depth of field', defined as the axial distance away from the focus plane that maintains 'sharpness' in the image within acceptable limits. This distance can be theoretically calculated as the sum of two components: a diffraction-limited term based on *NA*, wavelength (λ) and index of refraction (n); and a geometric (ray tracing) optics limitation based on sampling (pixel) size (e) and magnification (M) (Inoue and Spring 1997):

$$\mathrm{DOF} = \frac{\lambda \cdot n}{NA^2} + \frac{n}{M \times NA} e. \tag{6}$$

To avoid confusion with the traditional definition of 'depth of field', for macroscopic fluorescence imaging we use depth of integration (DOI) to quantify the depth at which a point source's intensity will decrease to a specified fraction. The depth contributing to the signal at a pixel is thus the DOI that corresponds to a loss of intensity below detectable limits.

A model of intensity profile over depth for a given lens can be obtained by examining how wide a point source spreads as it moves away from the focal plane, i.e. circle of confusion. If a point is substituted instead by a circular source with finite diameter, q, each point of the circle will project as a blur spot with diameter c when observed out of focus (figure 1(B), see the appendix). Thus, the resultant image is a larger circle of confusion with diameter $-Mq + c$ in which the original size is scaled by the magnification M (note that $M < 0$ for real, inverted images). If we further assume that the circular source emits an intensity of I_0 while in focus, then the average intensity of each point source in this circle (while in focus), $\widehat{I}$, is equal to I_0 divided by the area of the source in the image plane:

$$\widehat{I} = \frac{I_0}{\pi\left(\frac{-Mq}{2}\right)^2}. \tag{7}$$

For images away from the focal plane, the average intensity density (I) will be lower since it is distributed over a larger projected area:

$$I = \frac{I_0}{\pi\left(\frac{-Mq+c}{2}\right)^2}. \tag{8}$$

Intensity away from the focal plane can then be normalized by the intensity at the focal plane, $\widehat{I}$. After substituting the expression derived in the appendix (A.10) for the circle of confusion c, a relative intensity profile is obtained as a function of depth and three lens parameters: aperture a, magnification M and focal length f:

$$\frac{I}{\widehat{I}} = \frac{\frac{I_0}{\pi\left(\frac{-Mq+c}{2}\right)^2}}{\frac{I_0}{\pi\left(\frac{-Mq}{2}\right)^2}} = \frac{(-Mq)^2}{(-Mq+c)^2} = \frac{q^2}{\left(-q + aM\left|\frac{z}{Mf-f+zM}\right|\right)^2}. \tag{9}$$

Equation (9) can be solved for z, the distance from the focal plane, to calculate the depth of integration. For example, for an 80% drop in intensity, DOI_{80} can be determined from the two solutions ($z_{80,\mathrm{near}}$ and $z_{80,\mathrm{far}}$) where h is 0.2 for DOI_{80} and 0.1 for DOI_{90}, etc.:

$$z_{80,\mathrm{near}} = \frac{fq(\sqrt{h}-1)(M-1)}{M((a-q)\sqrt{h}+q)}, \qquad z_{80,\mathrm{far}} = \frac{fq(\sqrt{h}-1)(M-1)}{M(q-(a+q)\sqrt{h})}, \tag{10}$$

$$\mathrm{DOI}_{80} = (z_{80,\mathrm{far}} - z_{80,\mathrm{near}}) = \frac{2afq\sqrt{h}(\sqrt{h}-1)(M-1)}{a^2hM - (\sqrt{h}-1)^2Mq^2}. \tag{11}$$

Even though optical mapping is done with planar sensors lacking the ability to resolve point sources at varying depths, it is often desirable to know the limits of the depth of volume from which fluorescence is collected, and this can be considered a surrogate for depth resolution. We will employ the term 'axial spatial resolution' (ASR), as opposed to lateral spatial resolution (LSR) in the focal plane, to mean the limits to which a point source can be moved away from the focal plane and remain detectable (above background noise). By this definition, ASR is the limiting DOI for which the intensity falls below the noise floor (or the sensor's intensity resolution for a digital, noise-free system), equation (12).

$$\begin{aligned} &\mathrm{ASR} = \mathrm{DOI}_k \\ &k = \frac{\sigma}{S_{p-p}} \times 100\% = \frac{1}{\mathrm{SNR}} \times 100\%. \end{aligned} \tag{12}$$

So far we have considered the intensity profile in a vacuum. Fluorescence imaging of thick, 3D specimens will inevitably incur a loss of signal both from attenuation of excitation and emission light as well as photon scattering (Hyatt *et al* 2003, Bishop *et al* 2006). The collected fluorescence can be expressed as a function of tissue depth, z:

$$\begin{aligned} E_{\mathrm{em}} &= E_{\mathrm{ex}} Q E_{\mathrm{dye}} \, \mathrm{e}^{-\frac{z}{\delta_{\mathrm{em}}}} \\ E_{\mathrm{em}} &= \underbrace{I_0 \, \mathrm{e}^{-\frac{z}{\delta_{\mathrm{ex}}}}}_{E_{\mathrm{ex}}} \underbrace{Q Y_{\mathrm{dye}} (1 - 10^{-[\mathrm{dye}]\varepsilon})}_{Q E_{\mathrm{dye}}} \mathrm{e}^{-\frac{z}{\delta_{\mathrm{em}}}} \end{aligned} \tag{13}$$

where δ_{ex} and δ_{em} are the effective penetration depth for excitation light and the z-dimension emission range, respectively; QE_{dye} is the quantum efficiency of the fluorescent dye (photons emitted per photon absorbed); QY_{dye} is the quantum yield of the fluorescent dye, [dye] is the

local concentration of the fluorescent dye and ε is the extinction coefficient of the fluorescent dye.

When the properties of the fluorescent dye are not readily available, the effective depth of the contributing region to the measured intensities can be estimated using simplified mono- and bi-exponential models. This depth has been empirically and theoretically estimated to range from 0.25 to 1.5 mm (Girouard *et al* 1996, Baxter *et al* 2001). A simple expression for the excitation and emission profiles in depth has been proposed by Baxter *et al* which can be used to assess overall fluorescence intensity, $I(z)$ (Baxter *et al* 2001). We have slightly modified it here by normalizing with respect to intensity at the surface, $I(z = 0)$, equation (14), as opposed to integration over the entire tissue depth.

$$\begin{aligned} E_{\text{ex}} &= C_1 \, \mathrm{e}^{-\frac{k_1 z}{\delta_{\text{ex}}}} - C_2 \, \mathrm{e}^{-\frac{k_2 z}{\delta_{\text{ex}}}} \\ E_{\text{em}} &= C_3 \, \mathrm{e}^{-\frac{k_3 z}{\delta_{\text{em}}}} \\ I(z) &= \frac{E_{\text{ex}}(z) E_{\text{em}}(z)}{E_{\text{ex}}(0) E_{\text{em}}(0)}. \end{aligned} \tag{14}$$

3. Experimental methods

3.1. Sensor and lenses tested

All images were taken with Cooke pco.1200hs CMOS camera (Cooke Corp, Romulus, MI) having 1280 × 1024 (1.3 MP) 12 μm square pixels digitized at 10 bits per pixel with exposure times set to 45, 100 or 130 ms as indicated. Two fixed-focus 50 mm focal length lenses at approximately 0.5× magnification were used for lateral spatial resolution (LSR) testing: a Rodenstock TV-Heligon $f/0.75$ and a Navitar Platinum $f/1.0$. To assess the LSR of a tandem lens design (Ratzlaff and Grinvald 1991), a Nikkor 105 mm $f/2.0$ and a Nikkor 55 mm $f/2.8$ were focused at infinity, apertures fully open, and set facing each other to achieve approximately 0.52× magnification. Formation of a target image for LSR measurement was achieved through the use of a Nikkor 35 mm $f/1.4$ photographic lens focused to infinity and aperture full open. Axial spatial resolution (ASR) was examined with a Navitar 25 mm $f/0.95$ at about 1/10× magnification, maximum aperture and focus set to infinity.

3.2. Estimation of lens performance in macromode

Optical mapping systems often require low to medium magnification forcing the lens to be focused closer than the hyperfocal distance when the object can no longer be accurately considered to be located at infinity. Under these conditions, the published $F/\#$ for lenses overestimate the light gathering efficiency. A correction factor ('bellow's correction') can be used to estimate the loss of light via an increase in the effective $F/\#$, F_{eff}:

$$F_{\text{eff}} = F\left(1 + \frac{|M|}{p}\right). \tag{15}$$

In equation (15), the magnification M is used to judge departure from infinity focus where M approaches zero; p represents the entrance-to-exit pupil size ratio which is 1 for symmetric lenses. For magnifications $M > 1$, the increase in effective $F/\#$ is considerable (two times change at 1× magnification according to this simplified expression). We used a lens pre-design software from Linos Photonics (Milton, MA) to assess the deterioration in $F/\#$ due to macromode operation by specifying the fundamental lens parameters: focal length, infinity $F/\#$ and magnification (Linos Photonics GmbH 2006). In a tandem lens design,

the effective $F/\#$ depends on which of the two lenses functions as the aperture stop and on the magnification, M (ratio of the two focal lengths f_1 and f_2). Assuming simple lenses, the ability to have smaller (better) $F/\#$ in a tandem lens design comes from the effective focal length, f_{eff}, being shorter than that of the either individual lens, equation (16).

$$\frac{1}{f_{\text{eff}}} = \frac{1}{f_1} + \frac{1}{f_2}; \qquad a_1 = \frac{f_1}{F_1} \qquad \text{and} \qquad a_2 = \frac{f_2}{F_2}; \qquad M = \frac{f_2}{f_1}$$
$$F_{\text{eff}} = \frac{f_{\text{eff}}}{\min(a1, a2)} = \begin{cases} F_1\left(\frac{1}{\frac{1}{M}+1}\right) & \text{if} \quad a_1 \leqslant a_2 \\ F_2\left(\frac{1}{M+1}\right) & \text{if} \quad a_1 \geqslant a_2 \end{cases}. \tag{16}$$

3.3. Contrast transfer function (CTF) measurements

A 21 cm diameter resolution target pattern (Siemens star, 36 lp/circumference) was printed on a transparency film (CG5000, 3M) using a Lexmark T632 laser printer at 1200 dpi. The transparency was uniformly back illuminated by a 15.4″ WUXGA LCD screen displaying pure green at maximum backlight intensity. 1:75 reduction of the target image was achieved through the use of a Nikkor 35 mm $f/1.4$ as a projection lens to obtain a 2.8 mm diameter image at near hyperfocal distance (figure 2(A)). To more closely replicate optical mapping conditions and to ensure monochromatic responses, a 535 nm bandpass interference emission filter (Chroma) was placed in front of the camera. Using custom software in MATLAB (Mathworks), multiple circumferential intensity curves were extracted from captured images at different radii corresponding to different resolutions of the Siemens star. Median intensity was determined for each resolution and used as a threshold to classify 'high/bright' and 'low/dark' intensities. The ratio of the difference between the mean high ($I_{\max}$) and low ($I_{\min}$) intensity values to the sum of the two was used to construct relative CTF curves, i.e. per cent contrast (%C) as a function of spatial frequency, ν:

$$\%\text{C} = \frac{I_{\max}(\nu) - I_{\min}(\nu)}{I_{\max}(\nu) + I_{\min}(\nu)} \times 100. \tag{17}$$

3.4. Transmission efficiency

Transmission efficiency of the lenses was assessed by using the clear centre of the Siemens star testing pattern (5.7 mm in diameter in the real image and 58 μm in the projected image). Per cent transmission was calculated as a fraction of the intensity of the target image at different exposure times. Assuming constant target intensity over time, line fits were made to each data point across exposures with the y-intercept clamped to 0 to estimate the amount of light passing through the lens expressed as greyscale levels per millisecond (GL ms^{-1}).

3.5. Intensity profile over depth

Axial resolution for the Navitar 25 mm $f/0.95$ lens was probed with a 480 nm light emitting diode (LED) (Nichia, Japan) under a 1.3 neutral density filter simulating a quasi-monochromatic point source (figure 2(B)). From the focal plane (determined as the position generating the brightest and sharpest image), images were acquired at various distances and the average light intensity from the central 3 × 3 pixel region was calculated to yield an intensity profile over depth.

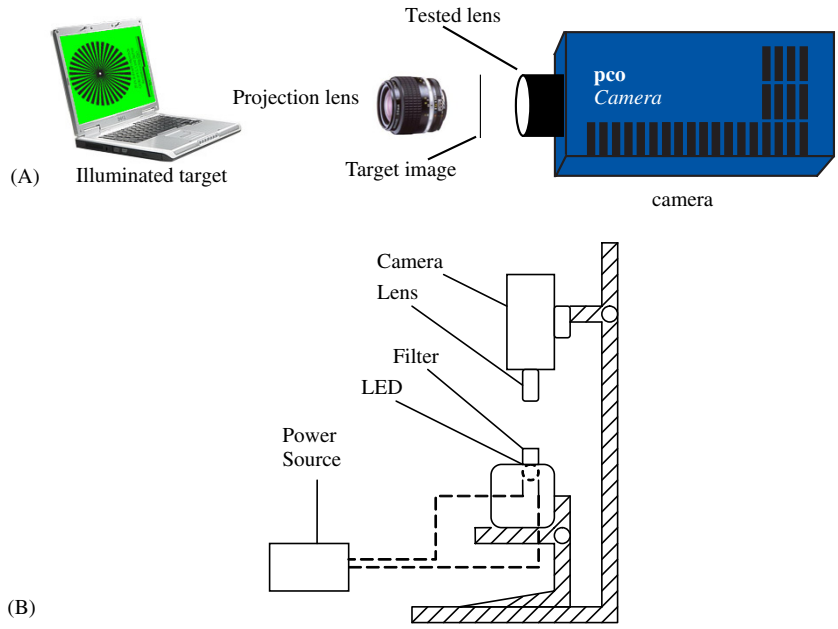

Figure 2. (A) Lens testing setup for obtaining CTF curves. A laptop back-lit LCD screen displaying pure green was used to illuminate a Siemens star pattern, which was further reduced 100× with a projection lens before being imaged at 0.5× magnification with the lens under test. (B) Lens testing setup for estimating depth of field (DOF) and depth of integration (DOI). A blue LED was mounted on a *Z*-stage for fine (<1 mm) adjustments while the camera was mounted to an adjustable rack for coarse (>1 cm) adjustments.

Table 1. Change in effective *F*-number, *NA* and collected light during macromode operation (expressed as a fraction of the light seen at the hyper-focal distance) at various magnifications for a subset of high-*NA* lenses.

Lens	Focal length	Magnification	$F/\#$ (infinity)	Effective $F/\#$	*NA*	% Intensity
Rodenstock	50	0.5×	0.75	1.13	0.406	44%
Navitar	25	0.5×	0.95	1.43	0.331	44%
Navitar	50	0.1×	1	1.1	0.414	83%
Navitar	50	0.5×	1	1.5	0.316	44%
Navitar	50	1×	1	2	0.242	25%
Navitar	50	2×	1	3	0.164	11%
Navitar	50	4×	1	5	0.100	4%

4. Results

4.1. Macromode imaging leads to NA deterioration

Theoretical predictions of the loss of light due to macromode imaging are summarized in table 1 for the lenses tested. Considering that image brightness is inversely proportional to the square of the $F/\#$, the per cent of light collected by a lens in macromode versus infinity focus can be expressed as the ratio of the infinity $F/\#$ squared to the effective $F/\#$ squared. Even for large aperture lenses such as the Navitar 50 mm $f/1$, operating at 1× magnification results in a quarter of light intensity. In comparison, for tandem lens setups in which both

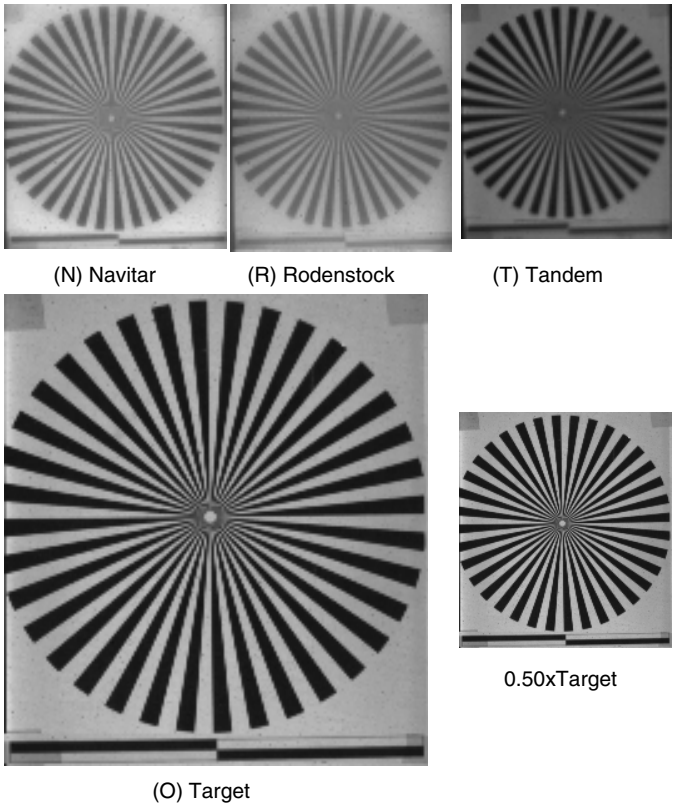

Figure 3. Images of the Siemens star pattern containing 36 black/white pairs around its circumference used for CTF estimation. Bottom scale bar is 10 cm per dark segment on the real target; both segments were used for determining magnification. The central portion of the Siemens star is clear and was used for estimation of transmission efficiency. All images shown are at 100 ms exposure time. (O) Target image generated by projection lens shown to scale. To the right is the same image reduced by 50% for comparison to tested lens images. The scale bar is 993 μm. (N) Target image viewed through Navitar 50 mm $f/1.0$ fixed focus lens at 0.52 $\times$ demagnification. Scale bar segment is thus 516 μm. (R) Target image viewed through Rodenstock TV-Heligon 50 mm $f/0.75$ lens at 0.52$\times$ demagnification. Scale bar segment is 513 μm. (T) Target image viewed through tandem lens assembly composed of Nikkor 105 mm $f/2.0$ and Nikkor 55 mm $f/2.8$, both focused at infinity, achieving 0.48 $\times$ demagnification. Scale bar segment is 479 μm.

lenses are focused at infinity, the effective $F/\#$ will be lower than the $F/\#$ of each individual lens with higher magnifications yielding better performance when the imaging (second) lens is the limiting aperture, equation (16). The calculations in table 1 assumed symmetric lenses with pupil magnification ratio $p = 1$. For most lenses, this is the best estimate given the lack of detailed design specifications, but asymmetric lenses with $p > 1$ are possible.

4.2. Numerical aperture alone does not predict lens resolution

Theoretically, the ability of a lens to preserve contrast at high spatial frequencies is directly proportional to its numerical aperture, quantified by the monochromatic diffraction-limited modulation transfer function (MDMTF), equation (3). However, our results (figures 3 and 4(A)) indicate that the Navitar 50 mm $f/1.0$ lens (effective $NA = 0.316$) slightly outperforms

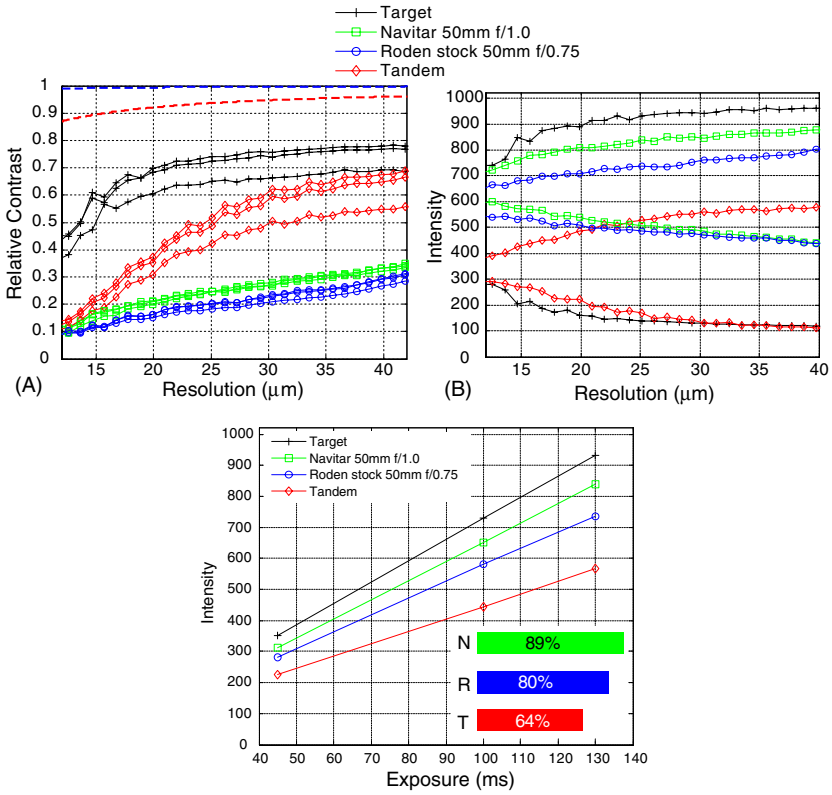

Figure 4. (A) Relative CTF curves for the tested lenses. For each lens, three exposure curves are shown: 130 ms, 100 ms and 45 ms. In all cases relative contrast decreased as exposure time decreased. Plotted is the per cent contrast (see the text for definition) at a given spatial resolution. Most lenses tested were relatively insensitive to exposure times with the exception of the tandem lens. Dashed lines indicate theoretical MDMTF curves for a 50 mm $f/0.75$ lens and for the tandem lens assembly. (B) Maximum and minimum intensities recorded for bright (high) and dark (low) areas show the relationship between overall brightness and contrast (normalized difference between high and low values). Maximum reportable intensity is 2^{10} or 1024; exposure time was 130 ms. (C) Transmission efficiency of selected lenses over different exposure times. Lines were fitted to greyscale intensity as a function of exposure time and slopes extracted in units of greyscale levels per millisecond (GL ms^{-1}). Each lens' slope was significantly different from the others (T: 3.4 GL ms^{-1}, R: 5.1 GL ms^{-1}, N: 5.5 GL ms^{-1}, $p < 0.05$). Insert: per cent transmission with respect to the original target is shown for the three lens configurations at 100 ms exposure.

the Rodenstock 50 mm $f/0.75$ (effective $NA = 0.406$) in the contrast transfer function test. Most surprising is the visibly superior contrast of the tandem lens system with an effective *NA* of just 0.176 despite the worst predicted MDMTF due to poor *NA* and multiplication of two MDMTF curves (one for each lens in the tandem lens pair).

Also noticeable in figure 3 is the brighter image in both 50 mm lenses compared to the tandem lens. Because the definition of per cent contrast penalizes brighter images by assuming perfectly dark backgrounds per equation (17), we plotted the raw greyscale values of bright ($I_{\max}$) and dark ($I_{\min}$) regions across spatial frequencies in figure 4(B) to see if the improved contrast of the tandem lens remained. In this view, the difference between bright and dark greyscales is very similar for the tandem and Navitar lenses indicating comparable

performance. Surprisingly, the lens with the highest *NA* (Rodenstock) had the worst contrast—percent-wise and as a raw difference.

When exposure time was varied from 130 ms to 45 ms, the CTF of the two 50 mm lenses did not change much, whereas the tandem lens suffered significant degradation of per cent contrast at shorter exposure times (figure 4(A)). Examination of the raw difference in intensity (figure 4(B)) explains why the tandem lens' contrast is limited by available light (dim image). As exposure time shortens, $I_{\min}$ and $I_{\max}$ curves for both the Navitar and Rodenstock decline but maintain their separation (absolute contrast) while the tandem lens assembly experiences compression of $I_{\max} - I_{\min}$ difference due to the inability of $I_{\min}$ to fall below the noise floor.

The dim image generated by the tandem lens might be attributed to its poor *NA*, but the Navitar lens still produces brighter images than the Rodenstock despite slightly worse *NA*. We quantified this loss of light by evaluating the per cent of light transmitted through the clear, central portion of the resolution target. As expected, the tandem lens resulted in only 64% of the original target intensity compared to 89% for the Navitar and 80% for the Rodenstock (figure 4(C)).

4.3. Contrast performance depends upon available light or exposure timing

The linear relationship between exposure time and intensity for each lens seen in figure 4(C) demonstrates the camera's linear response and permits one to extrapolate performance at faster exposure times more typical for optical mapping. The slope of each lens' intensity level as a function of exposure time (in units of greyscale levels per millisecond, GL ms^{-1}) predicts the loss of greyscale values for a given increase in the imaging rate. As noted earlier, contrast will remain the same as long as both $I_{\min}$ and $I_{\max}$ are permitted to decline. When the predicted greyscale levels dip below zero, reduction of contrast will occur since the camera cannot report negative greyscale values. For example, going from 130 ms to 5 ms (a reduction of 125 ms) will result in a loss of 3.4 GL ms^{-1} $\times$ 125 ms or 425 GL for the tandem lens, which exceeds the minimum black greyscale level of 100 and therefore would be reported as simply 0. The brightest region would be reduced from 600 GL to 175 GL resulting in maximum intensity differences of just 175 GL. Meanwhile, the Navitar lens would lose 688 GL reducing contrast from 500 GL to 212 GL, and achieving better contrast at 5 ms (212 GL versus 175 GL) than the tandem lens which previously excelled at 130 ms (500 GL versus 600 GL, respectively).

A comparison between various lenses can best be performed using background-adjusted CTF, figure 5. By subtracting the minimum black level from all signals yielding a mathematically perfect black background, CTF will always be 1 at very low spatial frequencies and gradually deteriorate as spatial frequencies increase. The CTF of the three lenses are now rather similar with the tandem lens starting at better CTF values until around 21 μm resolution where it rapidly falls below that of the Navitar and Rodenstock (these values should be divided by magnification to obtain the spatial resolution in the object plane). As expected from figure 3(B), the Navitar remained slightly better in contrast (it had greater absolute contrast) than the higher-*NA* Rodenstock lens throughout the tested range.

4.4. Lateral spatial resolution (LSR) in optical mapping depends on dye quality and SNR

Typical optical mapping recordings in our lab from monolayer cardiomyocyte cultures stained with Fluo-4, an intracellular calcium indicator dye, result in approximately 100 GL difference with the Navitar 50 mm $f/1.0$ lens at 0.5$\times$ magnification and a 10 bit sensor. The minimum detectable contrast is thus 1% (1 GL) in noise-free conditions, but at our typical signal-to-noise ratio (SNR) of 10, the minimum acceptable CTF is 10% to avoid falling below the noise floor,

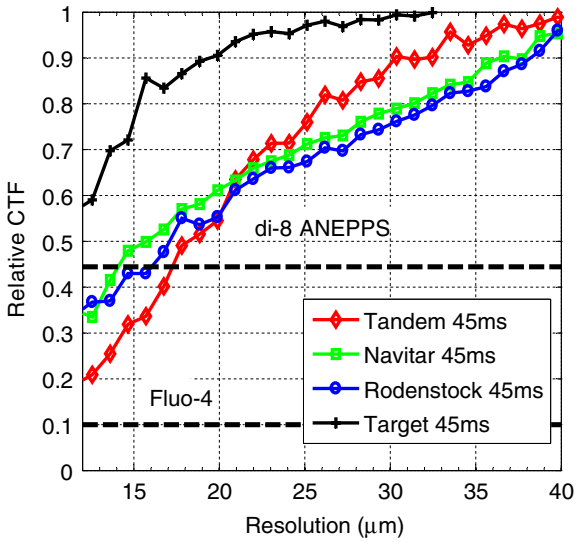

Figure 5. Deterioration of effective spatial resolution for different contrast conditions in the object. Background adjusted CTF is shown against spatial resolution in the image plane for each tested lens at 45 ms exposure (different exposures had no effect, data not shown). Broken horizontal lines indicate minimum acceptable contrast for Fluo-4 and di-8 ANEPPS fluorescent signals with SNR of 10 and 2.25, respectively. The absolute limit of spatial resolution is 12 μm—the size of the sensor pixel.

equation (5). From figure 5, it is clear that the Navitar lens' CTF does not fall below 10% at spatial frequencies up to the sensor resolution of 12 μm. Therefore, our LSR for Fluo-4 imaging is 24 μm (since we operate at 0.5$\times$ magnification) in discriminating the wavefront where signal amplitude is greatest. One can also determine the minimum SNR required before the lens will impose a limitation on LSR using equation (5). For both the Navitar and Rodenstock, the CTF at sensor resolution is approximately 0.35 yielding a minimum required SNR of 2.8 whereas the tandem lens requires at least SNR of 5 to fully utilize the sensor-provided resolution.

For imaging transmembrane voltage, we typically use fast-response potentiometric dyes such as di-8-ANEPPS. The poor response of these styryl dyes often yields SNR around 2.25 with peak-to-peak signal amplitudes of just 18 GL in our system. Under these conditions, the minimum acceptable CTF is 44.4% from equation (5) as depicted in figure 5. Such a high requirement results in optically limited LSR of 28 μm, 32 μm and 34 μm for the Navitar, Rodenstock and tandem lens, respectively (at 0.5$\times$ magnification) compared to the sensor LSR of 24 μm.

4.5. Axial spatial resolution (ASR) in optical mapping

For imaging thick specimens, the effective 'depth' seen by a pixel is determined by how fast light intensity falls off as the light source moves away from the focal plane. Due to space constraints, a shorter focal length lens, a Navitar 25 mm $f/0.95$, was used instead of the pair of 50 mm lenses tested above. Shown in figure 6 is the measured intensity profile for the 25 mm lens operated at 1/10$\times$ together with the predicted model from equation (9). Parameters a, M and f were known based on the lens specification, while the diameter of the source LED, q, was

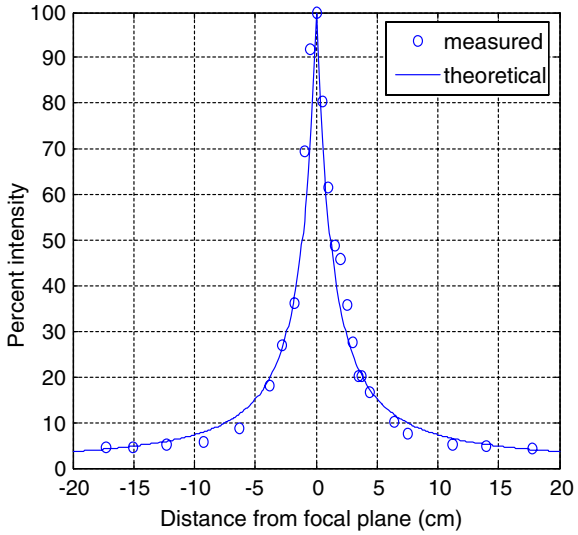

Figure 6. Experimental and theoretical estimation of DOI. Plotted are relative intensities as a function of distance from the focal plane; negative distances mean further away from the lens. Also shown is the theoretical curve of how intensity falls considering the size of the circle of confusion. A 25 mm $f/0.95$ lens was used at 1/10$\times$ magnification; the spot (LED) size at the focal plane was 2.88 mm. Note the excellent match of the empirical results with the theoretical predictions.

measured as 2.88 mm when focused. Note the excellent agreement between the theoretical curve and the experimental data.

As with LSR, the axial spatial resolution (ASR) is limited by the loss of intensity at distances away from the focal plane to the point where it falls below the noise floor; for perfectly noise-free systems the ASR becomes limited primarily by the intensity resolution (1 GL) and sensitivity of the sensor as specified by equation (12). Using the same examples as above, for intracellular calcium imaging with Fluo-4, SNR of 10, and a 50 mm $f/1.0$ lens, the ASR will be the combined distance away from the focal plane where the intensity falls to just 10% of its original value, DOI_{90} or 1.3 mm. The ASR for di-8-ANEPPS with SNR of 2.25 will be just 304 μm where intensity will have fallen to 44% (DOI_{56}) of the in-focus peak-to-peak signal amplitude. For comparison, in a noise-free, saturated (infinite contrast) system the ASR would be 18.4 mm before the signal drops below the 10 bit intensity resolution of the sensor ($\text{DOI}_{99.9}$).

4.6. Depth of field (DOF) does not correlate well with ASR

The theoretical DOF for an ideal point source using the effective *NA* of the 25 mm lens, magnification of 0.1$\times$ and pixel size of 12 μm can be calculated as 33 μm using equation (6). Yet, the empirically obtained DOF for a finite sized LED was 5 mm, estimated by occurrence of visible blurring. At this distance from the focal plane, the intensity dropped by only approximately 30% (figure 6) and thus light sources as far as 5 mm away would still be seen by the imaging sensor. Under ideal, noise-free saturating conditions the ASR for non-scattering, non-absorbing medium would be 6.5 cm or about an order of magnitude greater than the visually estimated DOF.

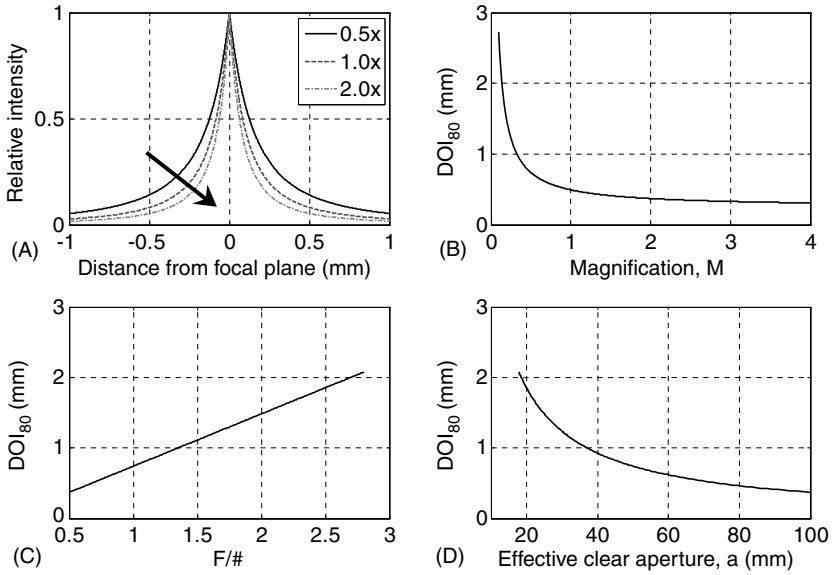

Figure 7. Characterization of depth of integration (DOI). (A) Plot of relative intensities as a function of distance from the focal plane for a 50 mm $f/1$ lens operated at three magnifications: $0.5\times$, $1\times$ and $2\times$. (B) Effects of magnification, M, on the depth of field, estimated by DOI_{80} (mm), equations (10) and (11), other lens parameters kept as in (A). (C) Effects of the lens F-number on the depth of field, estimated by DOI_{80} (mm). (D) Effects of the lens aperture, $a = f/\#F$, on the depth of field, estimated by DOI_{80} (mm).

4.7. Factors affecting axial spatial resolution (ASR)

The factors influencing DOI were further examined using the model described in equations (10) and (11) for a 0.1 mm point source imaged at different magnifications and apertures for DOI_{80}. Figure 7(A) presents the theoretical curves for a 50 mm $f/1$ lens at three magnifications: $0.5\times$, $1\times$ and $2\times$. The DOI_{80} (equations (10) and (11)) at $0.5\times$, $1\times$ and $2\times$ were 0.742 mm, 0.494 mm and 0.371 mm, respectively. Probing a range of magnifications yields the DOI_{80} curve shown in figure 7(B). For demagnification ($M < 1\times$), DOI_{80} increases rapidly to 2.72 mm at $1/10\times$. Small apertures also increase DOI_{80} as seen in figure 7(D). The usefulness of the $F/\#$ concept is illustrated by the nearly linear relationship when aperture is expressed as $F/\#$ in figure 7(C). Changes in focal length were found to have no effect on DOI_{80} (data not shown). The relative influence of magnification and F-number on DOI_{80} can be deduced from figure 8 depicting isolines for DOI_{80} over a range of practical magnifications and $F/\#$'s. Isolines more closely approaching horizontal (e.g. at high magnifications) indicate greater reliance of DOI on $F/\#$ than magnification, whereas nearly vertical isolines (e.g. at low magnification) demonstrate magnification's increasing influence.

4.8. Competing contributions of tissue attenuation and optics in determining ASR

The previous results have assumed uniform illumination throughout depth and no loss of fluorescence intensity as the signal emanates from deep within tissue. To address these issues, we used the simple model (equation (14)) described in Baxter *et al* (2001) for constructing a profile of fluorescence intensity for epicardial tissue ($C_1 = 927, C_2 = 702, C_3 = 1, k_1 = 1, k_2 =$

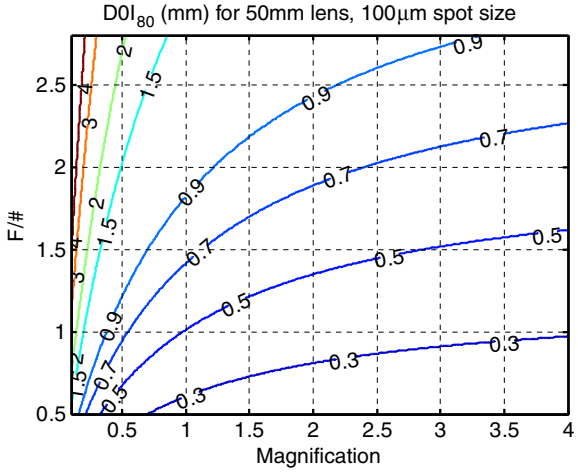

Figure 8. Combined effects of magnification and F-number on the depth of integration (DOI). Contour lines connect points with identical DOI_{80} (mm). A 50 mm lens and a 0.1 mm spot size are used in the calculations.

1.8, $k_3 = 1$, $\delta_{ex} = 0.71$ mm, $\delta_{em} = 1.33$ mm) ignoring the effects of optics ('no lens' curve in figure 9). To maintain consistency with our previous calculations of intensity profiles, we normalized the results to the intensity encountered at the surface ($z = 0$) where the focal plane is presumed to lie. Alongside, we plotted the model profile for a 0.1 mm point source with a 50 mm $f/1$ lens (figure 9(A)) at $1\times$ and $1/10\times$ magnification. Clearly, when compared to the intensity profile of tissue attenuation alone, the DOI is dominated by the quality of the lens. This assumes a small point-like source surrounded by darkness, but the smallest spacing expected in optical mapping of cardiac tissue is usually 1–2 mm (Mironov *et al* 2006). Repeating the same calculations for a 2 mm spot size (figure 9(B)) reverses the results such that tissue attenuation, not optics, determines DOI. Thus, the interplay of lenses, tissue properties and the propagation pattern determine how deep layers contribute to the measured signal at the surface. For a 0.1 mm spot size, high *NA* lenses operated at magnifications $M > 1\times$ have the ability to restrict the DOI to distances smaller than estimated from tissue absorption and scattering (figures 7–9). Even so, optical sectioning with resolutions better than 200 μm would be difficult without special confocality-facilitating techniques (Bernus *et al* 2005, Ramshesh and Knisley 2006), where the acquisition speed becomes a major issue.

5. Discussion and conclusions

Photographic lenses have been employed in optical mapping systems with broad-field illumination to escape the poor *NA* of low magnification microscope objectives. However, as $F/\#$ is appropriate only for infinite conjugate distances, a proper comparison between a microscope objective and photographic lens can only be achieved by converting the effective $F/\#$ for the expected operating conditions to numerical aperture used for conditions of finite conjugate distances (table 1). Furthermore, the use of *NA* and wavelength to determine spatial resolution is only accurate when diffraction is the limiting factor. Our results show that photographic and specialty lenses operated close-up often suffer loss of contrast at spatial

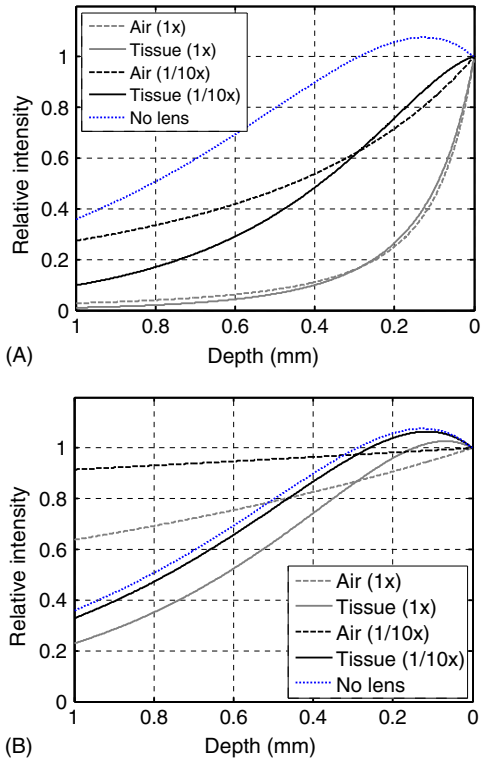

Figure 9. Combined effects of tissue scattering and optics on the depth of integration (DOI). (A) A 50 mm $f/1$ lens and a 0.1 mm spot were used in the calculations. (B) A 50 mm $f/1$ lens and a 2 mm spot were used in the calculations. Equation (14) was used to simulate the effects of tissue scattering and photon absorption ('no lens' curve). The optics-dictated drop in intensity for 'air' is shown in dashed lines for two magnifications ($M = 1/10\times$ and $1\times$). Finally, the 'no lens' tissue curves were convolved with the optics response to obtain how the lens would limit the DOI in tissue (solid curves for the two examined magnifications). Note the depth-limiting effect of the lens at $1\times$ magnification in (A), where a 0.1 mm point source was considered. When a 2 mm spot size was simulated in (B), the tissue absorption and scattering properties dominated the response regardless of lens characteristics and magnification.

frequencies outside the diffraction limits. Spatial resolution, therefore, becomes more a function of CTF and object contrast rather than a fixed value.

While the monochromatic diffraction-limited modulation transfer function (MDMTF) predicts better performance for larger aperture lenses, in practice subtle aberrations, e.g. stray light, can result in worse contrast as the aperture is widened. This is most clearly seen with photographic lenses where diffraction limited resolution occurs around $f/5$ or greater—opening such lenses wider (lower $F/\#$) results in loss of resolution from aberrations (Rosenbruch 1960). Similarly, specialty wide-aperture lenses, while collecting more light than 'slower' lenses, might optimize light gathering ability while sacrificing resolution. In this regard, the resolution of a lens does not necessarily follow its rated aperture as demonstrated here with the Navitar $f/1.0$ having better resolution than the Rodenstock $f/0.75$. Another possibility for the poor performance of the Rodenstock lens (having both worse transmission properties and resolution in spite of its superior *NA*) is the age of the lens. Improved manufacturing and engineering processes of modern lenses combined with the inevitable

flow of glass might have adversely affected the Rodenstock lens compared to the recently produced (2005) Navitar lens. Nevertheless, our results indicate that relying on the quoted $F/\#$ or NA of a lens to judge resolution may be misleading, and short of empirically testing each lens the actual resolution obtained is difficult to judge.

As previously reported, the use of two photographic lenses in a tandem-lens configuration (Ratzlaff and Grinvald 1991) can result in superior performance than either lens alone when focused closer than the hyperfocal distance. This is because there is no degradation of the rated F/# when the lenses are in infinity focus. However, the trade-off is the numerous glass elements that interpose between the object and the sensor, possibly reducing the total amount of light reaching in the sensor. Despite the individual lenses in the tandem lens setup having worse F/# than the Rodenstock and Navitar 50 mm fixed-focus lenses, the tandem lens has an effective focal length of just 36 mm with a 20 mm aperture stop (limited by the 55 mm $f/2.8$ lens) yielding a composite $F/\#$ of 1.84. Compared to the $f/1.5$ of the Navitar lens operated at 0.5× magnification (table 1), the tandem lens should result in 59% transmission versus 89% of Navitar's lens. The tandem lens' measured transmission of 64% indicates that the additional glass elements might not have played a substantial role, but without physically testing such a lens it is difficult to say whether an equivalently sized aperture tandem lens will outperform a single lens.

Ideally, CTF curves are measured with a detector having infinite resolution and monochromatic diffraction-limited operation. With a 12 μm square pixel, the camera used here for testing would be expected to exhibit decreasing contrast for spatial features less than 12–24 μm. This is reflected in the CTF curve for the projected target image where contrast begins to fall sharply around 15–20 μm (figure 4). The loss of contrast for all tested lenses at approximately 35 μm indicates the increasing impact that optics has on spatial resolution for detectors with pixel sizes smaller than 35 μm. Note that this finding is independent of magnification since all measurements refer to the image plane (i.e. for 0.5× magnification all values on the x-axis need to be multiplied by two to obtain actual resolution in the object). The background adjusted CTF curves in figure 5 hint at steadily decreasing contrast even with spatial frequencies as low as 40 μm (the largest tested feature size). While some detectors in optical mapping have larger pixel sizes, especially photodiode arrays, some modern CCD and CMOS imagers in use have pixel sizes around 8 μm and as small as 2.3 μm. Thus, the use of detector pixel size to determine spatial resolution is not always valid.

Even with relatively large pixel sizes, poor object contrast can significantly impair LSR. In optical mapping, poor contrast in the specimen is a reflection of low signal amplitude and/or low signal-to-noise ratios (SNR). One of the key determinants in signal amplitude and SNR is the dye response—the styryl potentiometric dyes are notorious for their weak fractional response, whereas the newer calcium dyes can generate intensity changes more than 100% of baseline fluorescence. For example, while the high contrast Fluo-4 optical data can achieve LSR better than our sensor's 12 μm pixels, di-8-ANEPPS becomes optically limited at 14–17 μm in the imaging plane (the actual resolution is 28–34 μm for 0.5× de-magnification).

The limitations of contrast on LSR come about mainly through the discrete nature of digital imaging systems as the ability to resolve between different intensities is limited by the amount of light needed to change 1 GL. For most systems, this is a function of dark noise and the bit-resolution of the sensor; however techniques such as removal of background bias via AC-coupling in photodiode arrays (PDAs) can dramatically extend the effective dynamic range (Obaid *et al* 1999) and thus intensity resolution. It should be noted, however, that 'background' as used in this paper refers mostly to the 'resting' fluorescence level of the specimen and not ambient light or other noise sources. Contrast in optical mapping is focused primarily on differences between 'resting' and 'excited' fluorescence.

The importance of knowing the actual LSR achieved is highlighted in recent reports on the spatiotemporal frequencies found in cardiac tissue (Mironov *et al* 2006, Bien *et al* 2006) where the highest spatial frequency, found at the wavefront where resting cells transition to the excited state, was measured to be in the range of 1–2 mm for a broad range of conditions. We must be confident, however, that our imaging system's LSR is capable of much finer detail. Some verification might come about from imaging other-than-normal propagation patterns, e.g. re-entrant spirals, where conduction velocity falls and high spatial frequencies can be found (Bien *et al* 2006). When such opportunities are not feasible or practical, as in the on-going debate over pin-wheels in the visual cortex (Polimeni *et al* 2005), empirical testing such as done here for our imaging system can serve to demonstrate the capability of detecting very fine spatial features. Moreover, the discussion and analysis so far have focused on the wavefront where the contrast is greatest. For optical mapping of repolarization, the contrast is significantly worse and the LSR can rapidly degrade.

When the analysis of resolution is extended to three-dimensional preparations, depth-resolved imaging requires thin optical sections. In this sense, the use of the word 'resolution' is a misnomer as one measures not the distance between two point sources along the optical axis (depth) where they can no longer be distinguished, but rather the limits of observing a point source away from the focal plane. Using this definition, point sources far away from the focal plane might still be detectable above the image noise, but the lateral localization of such a point will be extremely poor. For instance, an infinitely small point source 1 mm away from the focal plane of a 50 mm $f/1$ lens will project a circle of confusion 0.295 mm wide at $0.7\times$ magnification, or 4.1 mm at $5\times$ magnification. Unfortunately, without additional information, such fluorescence signals may be ambiguously interpreted as broad (low spatial frequency) activity in the focal plane, or deeper fine (high spatial frequency) activation.

Although admittedly simple models of light attenuation due to tissue were used here, the results indicate that depending upon the magnification and aperture of the lens employed as well as the size of the fluorescent region, optical 'sectioning' can be limited either by failure to excite/capture emitted fluorescence (tissue effects) or by the numerical aperture (lens effects). More complex models, such as photon diffusion simulations that include the effects of lateral light scatter coupled with detailed ionic models of electrical activity, have recently been published (Hyatt *et al* 2003, Bishop *et al* 2006), but they ignore the impact of lenses. The adverse impact of lateral scatter on LSR is expected to be greater for thick tissue than thin, monolayer specimens. Moreover, lateral scattering may also affect the intensity profile over depth and ASR in a complex fashion dependent upon the distribution of light sources in depth. Given the simplicity of our lens performance model, it would be relatively straightforward to couple these results with already developed photon-diffusion models of light–tissue interactions in order to obtain a more precise assessment of the relative contribution of scattering to image resolution.

In summary, our analysis shows that LSR and ASR achieved by an optical mapping system vary according to the conditions of imaging and the optics employed. This is an important point when interpreting optical signals and considering filtering parameters to improve signal quality. Theoretical predictions for ASR and LSR can only be made for assumed fluorescence intensity distributions in 3D space and time, depending on spatial frequency/contrast and location of the object (electrical waves) with respect to the focal plane. The constantly changing patterns of propagation in cardiac tissue in 3D space (Choi and Salama 1998, Efimov and Mazgalev 1998) make estimation of the dynamically variable LSR and ASR a very challenging task. For solving the inverse problem, i.e. predicting depth-resolved patterns from optical mapping on the surface, one may need to also consider optics and detector performance in addition to previously explored factors related to dye–tissue interactions and tissue scattering. For proper

interpretation of optical mapping results, one needs to be confident of the lower bound of LSR and ASR.

Acknowledgments

This work was supported in part by grants from The National Science Foundation (BES-0503336), The Whitaker Foundation (RG-02-0654) and the American Heart Association (0430307N) to EE, and a National Research Service Award to HB (1F30ES01337101).

Appendix. Circle of confusion

The term 'circle of confusion' refers to the non-confocal nature of regular lens-mediated image formation. A three-dimensional cone of light exists in the image domain in response to a point object on the optical axis of the lens. This is seen as a blur spot (the point spread function in the image plane) reflecting contributions by points on the optical axis but outside the focal plane. For each of these out-of-focus points, the equivalent in the image plane will not be a point but rather a circle with energy spread over an area.

Based on simple geometrical considerations and ray tracing, the size of the circle of confusion can be estimated using the classic lensmaker equation, which relates the lens–object distance s to the lens–image distance d in a lens with a focal length f. We adopt the convention for strictly positive values of s and d.

$$\frac{1}{s} + \frac{1}{d} = \frac{1}{f}. \tag{A.1}$$

As depicted in figure 1(A), given an ideal lens, one with no aberrations present, a point at the s-plane would focus onto an infinitesimally small point at the d-plane. A point in front of s at a distance s_f (distance measured from the lens) will focus behind d at a distance d_f. In the d-plane of the image, the point would be out of focus and would be seen as a circle (i.e. circle of confusion) with diameter c_f. Similarly, a point behind s at a distance s_r, focuses in front of d at a distance d_r. Its circle of confusion at d has a diameter c_r.

For a point at s_f, the diameter of the imaged circle of confusion, c_f, can be calculated using the following expression, in which a represents the aperture diameter of the lens:

$$c_f = a \left| \frac{d_f - d}{d_f} \right|. \tag{A.2}$$

By combining equations (A.1) and (A.2), the size of the circle of confusion can be expressed as a function of the distance z from the s-plane (the focal plane):

$$c_f = a \left| 1 - d \left(\frac{1}{f} - \frac{1}{s - z} \right) \right|. \tag{A.3}$$

Similarly, for a given object at a point s_r, the diameter, c_r, of the imaged circle of confusion can be calculated using equation (A.4), which can be further simplified to equation (A.5):

$$c_r = a \left| \frac{d - d_r}{d_r} \right| \tag{A.4}$$

$$c_r = a \left| d \left(\frac{1}{f} - \frac{1}{s + z} \right) - 1 \right|. \tag{A.5}$$

As evident from equations (A.3) and (A.5), c_f and c_r are equivalent for any given distance z. Hence, we define the diameter of the circle of confusion, c, as follows:

$$c = c_f = c_r = a\left|1 - d\left(\frac{1}{f} - \frac{1}{s+z}\right)\right|. \tag{A.6}$$

Furthermore, we can combine the lens maker equation (A.1) with an expression for the lens magnification, M (A.7), to obtain new expressions for s and d:

$$M = \frac{f}{f-s} = \frac{-d}{s} \tag{A.7}$$

$$s = \frac{(M-1)f}{M} \tag{A.8}$$

$$d = -(M-1)f. \tag{A.9}$$

Substituting (A.8) and (A.9) into equation (A.6) yields a new expression for the circle of confusion, which depends on three lens parameters: aperture, a, magnification, M and focal length, f:

$$c = aM^2\left|\frac{z}{Mf - f + zM}\right|. \tag{A.10}$$

References

Baxter W T, Mironov S F, Zaitsev A V, Jalife J and Pertsov A M 2001 Visualizing excitation waves inside cardiac muscle using transillumination *Biophys. J.* **80** 516–30

Bernus O, Wellner M, Mironov S F and Pertsov A M 2005 Simulation of voltage-sensitive optical signals in three-dimensional slabs of cardiac tissue: application to transillumination and coaxial imaging methods *Phys. Med. Biol.* **50** 215–29

Bien H, Entcheva E, Pertsov A, Mironov S and Vetter F 2006 Spatial frequency content in optical mapping of cardiac cell monolayers *Am. J. Physiol Heart Circ. Physiol.* **291** H1484–H1485

Bishop M J, Rodriguez B, Eason J, Whiteley J P, Trayanova N and Gavaghan D J 2006 Synthesis of voltage-sensitive optical signals: application to panoramic optical mapping *Biophys. J.* **90** 2938–45

Bray M A and Wikswo J P 2003 Examination of optical depth effects on fluorescence imaging of cardiac propagation *Biophys. J.* **85** 4134–45

Choi B R and Salama G 1998 Optical mapping of atrioventricular node reveals a conduction barrier between atrial and nodal cells *Am. J. Physiol.* **274** H829–H845

Coltman J W 1954 The specification of imaging properties by response to a sine wave input *J. Opt. Soc. Am.* **44** 468–71

Ding L, Splinter R and Knisley S B 2001 Quantifying spatial localization of optical mapping using Monte Carlo simulations *IEEE Trans. Biomed. Eng* **48** 1098–107

Efimov I and Mazgalev T 1998 High-resolution, three-dimensional fluorescent imaging reveals multilayer conduction pattern in the atrioventricular node *Circulation* **98** 54–7

Efimov I R, Nikolski V P and Salama G 2004 Optical imaging of the heart *Circ Res.* **95** 21–33

Entcheva E and Bien H 2006 Macroscopic optical mapping of excitation in cardiac cell networks with ultra-high spatiotemporal resolution *Prog. Biophys. Mol. Biol.* **92** 232–57

Girouard S D, Laurita K and Rosenbaum D 1996 Unique properties of cardiac action potentials recorded with voltage-sensitive dyes *J. Cardiovasc. Electrophysiol.* **7** 1024–38

Hyatt C J, Mironov S F, Wellner M, Berenfeld O, Popp A K, Weitz D A, Jalife J and Pertsov A M 2003 Synthesis of voltage-sensitive fluorescence signals from three-dimensional myocardial activation patterns *Biophys. J.* **85** 2673–83

Inoue S and Spring K R 1997 Video microscopy *The Fundamentals* (New York: Plenum)

Linos Photonics GmbH Linos Pre-designer 2006 Linos Photonics

Mironov S F, Vetter F J and Pertsov A M 2006 Fluorescence imaging of cardiac propagation: spectral properties and filtering of optical action potentials *Am. J. Physiol. Heart Circ. Physiol.* **291** H327–35

Obaid A L, Koyano T, Lindstrom J, Sakai T and Salzberg B M 1999 Spatiotemporal patterns of activity in an intact mammalian network with single-cell resolution: optical studies of nicotinic activity in an enteric plexus *J. Neurosci.* **19** 3073–93

Polimeni J R, Granquist-Fraser D, Wood R J and Schwartz E L 2005 Physical limits to spatial resolution of optical recording: clarifying the spatial structure of cortical hypercolumns *Proc. Natl Acad. Sci. USA* **102** 4158–63

Ramshesh V K and Knisley S B 2003 Spatial localization of cardiac optical mapping with multiphoton excitation *J. Biomed. Opt.* **8** 253–9

Ramshesh V K and Knisley S B 2006 Use of light absorbers to alter optical interrogation with epi-illumination and transillumination in three-dimensional cardiac models *J. Biomed. Opt.* **11** 24019

Ratzlaff E H and Grinvald A 1991 A tandem-lens epifluorescence macroscope: hundred-fold brightness advantage for wide-field imaging *J. Neurosci. Methods* **36** 127–37

Rosenbruch K J 1960 Die optischen Bildfehler und die Uebertragungsfunktion *Optik* **17** 249–77

Smith W J 1990 *Modern Optical Engineering* (Boston, MA: McGraw-Hill)

Endnotes

(1) Author: The cost of printing a single page in colour is 475 GBP. Each additional page costs 95 GBP. Please let us know if you would like to cover this cost, or if you would prefer colour to appear in the electronic version only.
